Mechanisms of cracking and delamination within thick thermal barrier systems in aero-engines subject to calcium-magnesium-alumino-silicate (CMAS) penetration

S. Krämer [a,*], S. Faulhaber [a], M. Chambers [a], D.R. Clarke [a],
C.G. Levi [a], J.W. Hutchinson [b], A.G. Evans [a]

[a] *Materials Department, University of California, Santa Barbara, CA 93106-5050, United States*
[b] *Division of Engineering and Applied Science, Harvard University, Cambridge, MA 02138, United States*

Abstract

An analysis has been conducted that characterizes the susceptibility to delamination of thermal barrier coated (TBC) hot-section aero-turbine components when penetrated by calcium-magnesium-alumino-silicate (CMAS). The assessment has been conducted on stationary components (especially shrouds) with relatively thick TBCs after removal from aero-engines. In those segments that experience the highest temperatures, the CMAS melts, penetrates to a depth about half the coating thickness, and infiltrates all open areas. Therein the TBC develops channel cracks and sub-surface delaminations, as well as spalls. Estimates of the residual stress gradients made on cross-sections (by using the Raman peak shift) indicate tension at the surface, becoming compressive below. By invoking mechanics relevant to the thermo-elastic stresses upon cooling, as well as the propagation of channel cracks and delaminations, a scenario has been presented that rationalizes these experimental findings. Self-consistent estimates of the stress and temperature gradients are presented as well as predictions of channel cracking and delamination upon cooling.
© 2008 Elsevier B.V. All rights reserved.

Keywords: Thermal barrier coatings; Delamination; Thermal gradients; Cracking; Environmental degradation

1. Introduction

The maximum temperature capability of thermal barrier systems used in gas turbines is often limited by deposits of calcium-magnesium-alumino-silicate (CMAS) [1–3]. These deposits melt and wet the yttria-stabilized zirconia (YSZ) used as the thermal barrier coating (TBC), causing it to be drawn by capillarity into all of the open void space [1]. Upon cooling, when the CMAS solidifies, the penetrated layer develops a high modulus [1]. Those regions penetrated by CMAS are detrimental since TBCs rely on spatially configured voids which increase the strain tolerance with the superalloy substrate as well as decrease thermal conductivity [4–6]. The consequences to airfoil durability have been documented for a system with a TBC generated by electron beam physical vapor deposition (EB-PVD) [2]. That assessment ascertained that the CMAS-penetrated layer is susceptible to delamination when subjected to subsequent rapid cooling.

The present investigation augments the previous study by analyzing the delamination mechanisms that occur in stationary components, such as shrouds (Fig. 1), with a thick TBC ($H \approx 1$ mm, Fig. 2) deposited by atmospheric plasma spray (APS). After use in an engine, some areas spall (Fig. 1). Regions in the proximity of the spalls have been investigated to assess the mechanisms and to establish the role of CMAS.

The intent of this article is to develop a mechanism-based correlation between CMAS penetration and TBC delamination. It has three parts. (i) The CMAS within the penetrated region is characterized by using scanning electron (SEM), optical and transmission electron (TEM) microscopy. This assessment provides an understanding of the depth of penetration of the CMAS relative to its melting temperature, crystallinity and viscosity. (ii) The residual stress gradients are estimated by using Raman piezo-spectroscopy. (iii) A synopsis of the mechanics relevant to thermo-elastic stresses, cracking in stress gradients and coating delamination is used to establish a crack-

* Corresponding author. Tel.: +1 805 893 8390; fax: +1 805 893 8486.
E-mail address: skraemer@engineering.ucsb.edu (S. Krämer).

Fig. 1. Plan view optical image of a segment of a turbine shroud. Three of the zones examined are indicated, as well as the (vertical) plane of cross-sectioning.
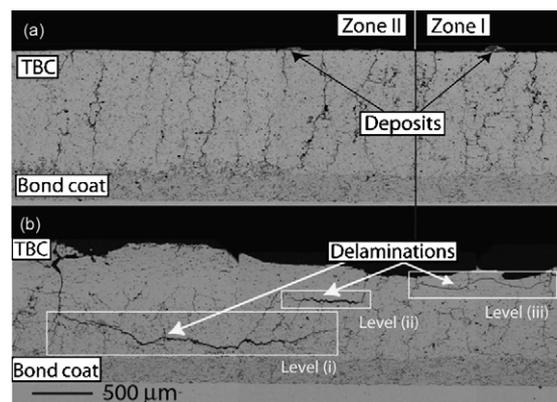
Fig. 2. Micrographs of cross-sections through the TBC along the plane marked in Fig. 1: (a) SE images of zones I and II. Note the dense vertical cracks (DVC) with spacing, $d = 0.2$ mm, and the deposits on the surface. (b) SE image of zone III close to the spalled region. Delaminations at three different levels are apparent. In each case the delaminations originate from channel cracks with separation, $s \sim 1$ mm (see Fig. 3 for details on channel crack morphology).

ing → delamination → spalling scenario that rationalizes and quantifies the measurements and observations.

The terminology used in this article is summarized in Table 1 and defined in the text. Briefly, the plan view of a segment cut from a representative shroud (Fig. 1) indicates three distinct *zones* (denoted I, II and III). Spalls are present in zone III, as well as sub-surface delaminations (Fig. 2b). The delaminations within this zone occur at three *levels* identified in figure.

2. Crack morphologies

Sections normal to the surface were made using procedures described elsewhere [7]. Scanning electron and optical images (Figs. 2 and 3) summarize the various crack and delamination morphologies. Plan view optical images of planarized surfaces (Fig. 3a and b) provide complementary information.

Zones I and II exhibit a characteristic splat microstructure [8] with an array of through-thickness separations typical of "dense vertically cracked" (DVC) systems [9–11]. The DVCs have spacing, $d \approx 0.2$ mm (Figs. 2a and 3a). The TBC has its original (as-deposited) thickness and a thin deposit is superposed.

Table 1
Terminology used to describe features of the material

Feature	Terminology	Significance
Affected area of shroud	Zone I	Shallow CMAS penetration
	Zone II	
	Zone III	Deep penetration of CMAS
Location of delamination	Level (i)	Just above bond coat
	Level (ii)	Just below CMAS
	Level (iii)	Just beneath surface
Region of CMAS penetration	Sublayer A	Upper region near-surface
	Sublayer B	Lower region of CMAS
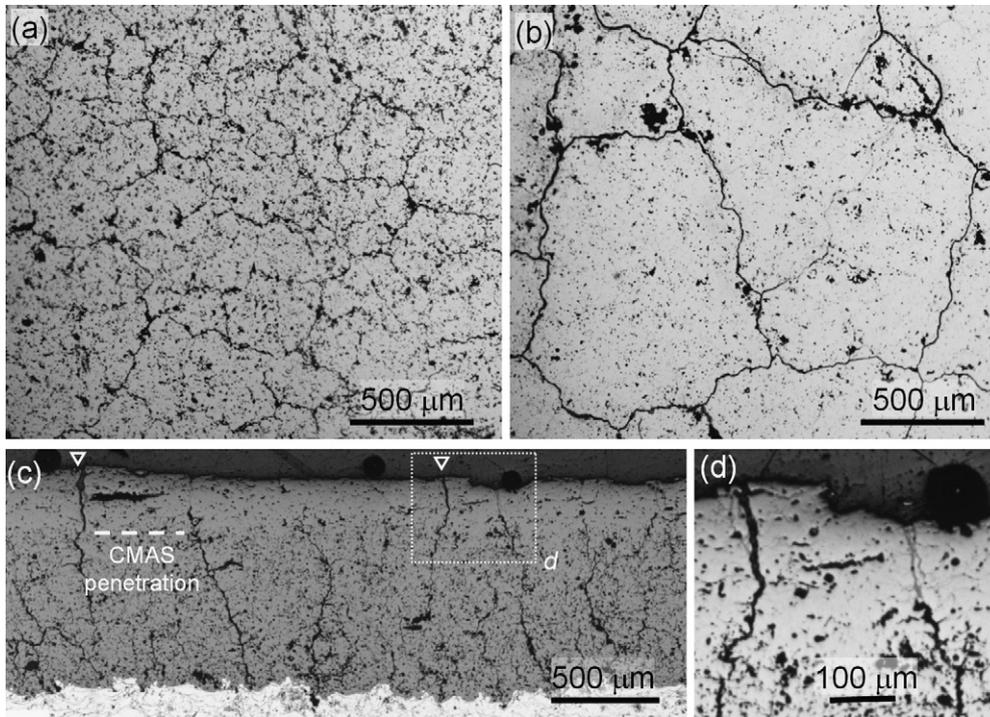
Fig. 3. Plan view optical micrographs of planarized surfaces in zone I (a) and zone III (b) in a region displaced from the spalled region. Zone I is characterized by a irregular pattern of DVC cracks with spacing of order ~200 nm. In zone III a network of pronounced channel cracks developed with spacing of order 1 mm. (c) Corresponding cross-sectional view of zone III showing two channel cracks (indicated by arrows). Note that the other DVCs are filled with CMAS throughout the penetration depth. The channel cracks form within prior DVCs, as indicated in magnified section (d).

The zones differ only in the surface roughness: zone II being much smoother (Fig. 1).

Zone III is characterized by extensive infiltration of CMAS, apparent from the contrast in Figs. 3c and d and 5. The DVCs are completely filled with CMAS wherever it penetrates (Fig. 3c and d). *Open* vertical cracks are also in evidence, starting at the surface and extending partially or fully through the penetrated layer (Fig. 3c). These (hereafter referred to as *channel cracks*) are quite uniformly separated, with spacing $s \approx 1$ mm (or $s/H \approx 1$) substantially larger than the DVC spacing. The plan view (Fig. 3b) indicates that these cracks are open and form a characteristic mud-crack pattern typical of thermal stress cracks generated on cooling. Moreover, the cross-sections (Fig. 3c) indicate that the channel cracks initiate and propagate substantially within the CMAS-filled DVCs.

The depth of CMAS penetration is location dependant. Close to the spalled region (Fig. 2b), $h \approx 500$ μm ($h/H \approx 0.5$). The penetration is shallower further away (Fig. 3c). In the deeply penetrated region, multiple sub-surface delaminations are evident: all originate from the extremity of one of the channel cracks (not the DVCs). They are located at three primary levels: (i) just above the bond coat, (ii) adjacent to the bottom of the CMAS-penetrated layer and (iii) just below the top surface. Those at level (iii) are filled with CMAS. Level (ii) delaminations often link causing a section of the penetrated material to spall, resulting in a "slab" of ejected material. Level (i) delaminations are extremely long and especially detrimental to the durability of the TBC. The most important characteristics of the channel cracks and delaminations are summarized in the schematic in Fig. 4.
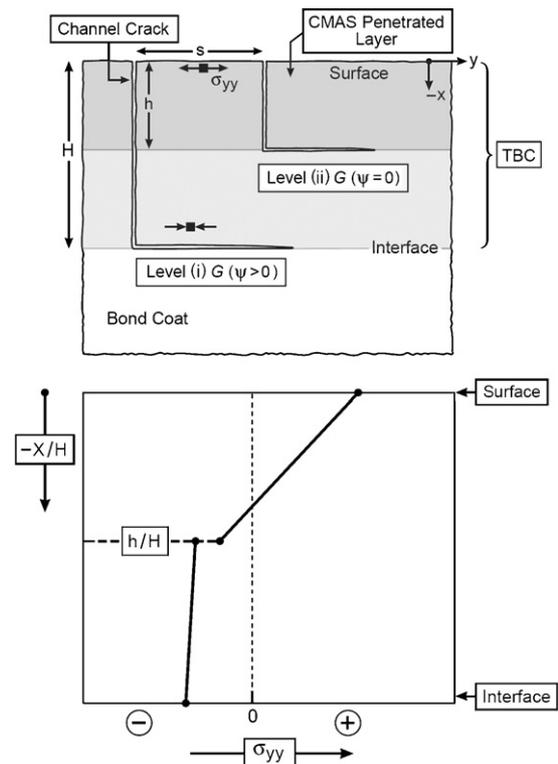
Fig. 4. A schematic indicating levels (i) and (ii) delaminations that develop from channel cracks as well as the associated stress distribution in the TBC (see Fig. 9 for the experimental substantiation of the stress distribution).

Table 2
Compositions in various regions of the shroud measured with SEM EDS

		Mg	Al	Si	Ca	Ti	Cr	Fe	Co	Ni	Y	Zr
Deposits on surface	Zone I	11	15	39	26	–	–	–	–	–	–	–
	Zone II	5	27	24	12	–	3	2	1	15	1	9
	Zone III	26	60	9	5	–	–	?	–	–	–	–
TBC	Original	–	–	–	–	–	–	–	–	–	9	91
	Spheroidized	–	–	–	6	1	–	2	–	–	10	80
CMAS penetrated TBC (distance from surface)	0 μm (a)	9	20	38	29	2	–	3	–	-	1	3
	130 μm (a)	9	17	38	31	2	–	3	–	–	1	3
	180 μm (c)	13.5	20	35	26	1	–	6	–	–	1	4
	350 μm (c)	16.5	13	42	26	1	–	3	–	–	1	3

Note: values for the CMAS-infiltrated material and the unaffected TBC were collected from zone III. The amorphous and crystalline CMAS are denoted (a) and (c), respectively. Linear gradients in composition were found in both.

The crack and delamination patterns in Fig. 4 suggest that, where the CMAS has penetrated to $h/H \approx 0.5$, tensile stress develops at the surface on cooling [12], causing channel cracks to form and extend (fully or partially) through the penetrated layer. On further cooling, the energy release rates on the level (ii) plane become large enough that (mode I) delaminations form from the channel cracks and extend adjacent to the CMAS layer. Thereafter, the energy release rate on the level (i) plane becomes large enough to extend delaminations from deep channel cracks, just above the bond coat (in mixed mode). A corollary is that there must be a critical CMAS penetration depth, below which the TBC does not delaminate.

3. Calcium-magnesium-alumino-silicate infiltration

Micro-chemical characterization was performed by EDS/SEM both on the residual surface deposits in the three zones, as well as the CMAS penetrated regions within zone III (typically along the trajectory of the DVCs), as summarized in Table 2. The deposits in zone I contain only the CMAS oxides, originating from debris ingested with intake air. Those in zone II also contain Ni, Co, Cr and Y, corresponding to compositions associated with the superalloy and the YSZ, implying that this zone has been subjected to abrasion by the airfoils (in accordance with the smoother surface: Fig. 1). The surface deposits on Zone III exhibit large fractions of Mg and Al (in a 1:2 ratio), suggestive of spinel, as well as small amounts of Si and Ca. It is presumed that the putative spinel is the solid residue left behind when the molten CMAS penetrated the coating.

The CMAS penetrated region in zone III (Fig. 5) can be divided into two sublayers. Channeling contrast images (Fig. 6) reveal that the lower part of the penetrated region (*sublayer* B in Figs. 5 and 6b) has microstructure similar to the unpenetrated TBC (Fig. 6c), except that the void space has been replaced by solidified CMAS. Moreover, some of the columnar grain boundaries internal to the splats have been penetrated. Quantitative analysis of the TBC microstructure using Fig. 6b reveals that the volume fraction of CMAS-filled porosity is $f = 0.2$. At locations nearer the surface (*sublayer* A in Figs. 5 and 6a), the filled features are spheroidized (rather than elongated) and
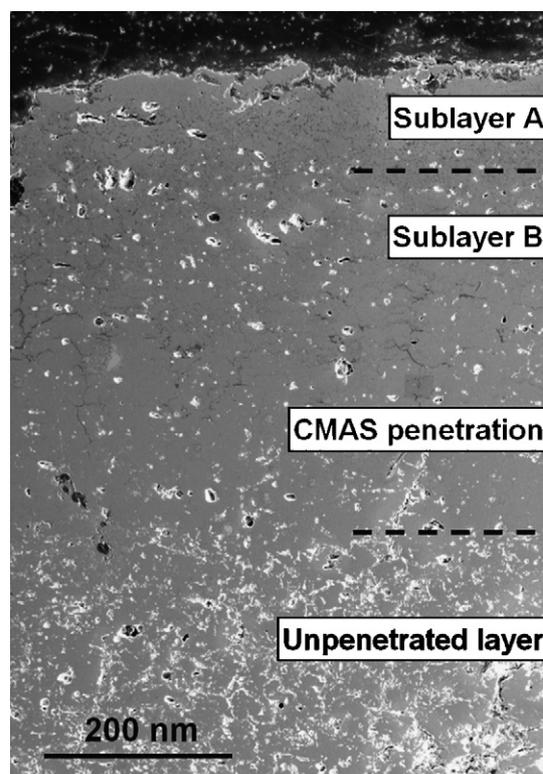

Fig. 5. Higher resolution SE image of a section within zone III that experiences minimal spalling, revealing the CMAS penetrated zone. This zone has two sub-regions (cf. Figs. 6 and 7).

contain globular particles with significantly different compositions than the original YSZ (Table 2). The incorporation of Ca (plus minor amounts of Ti and Fe) suggests a CMAS-melt mediated dissolution/re-precipitation mechanism [1] with features and underlying principles discussed in detail in a related study [3]. Analysis of the near-surface layer by X-ray diffraction and Raman indicates that the YSZ remains tetragonal, with no evidence of the cubic phase and minimal monoclinic phase.[1] The inference is that the extent of dissolution-re-precipitation is much less significant than in previous studies, presumably

---

[1] Significant cubic phase domains were found in another shroud. The implications will be discussed in a forthcoming publication.
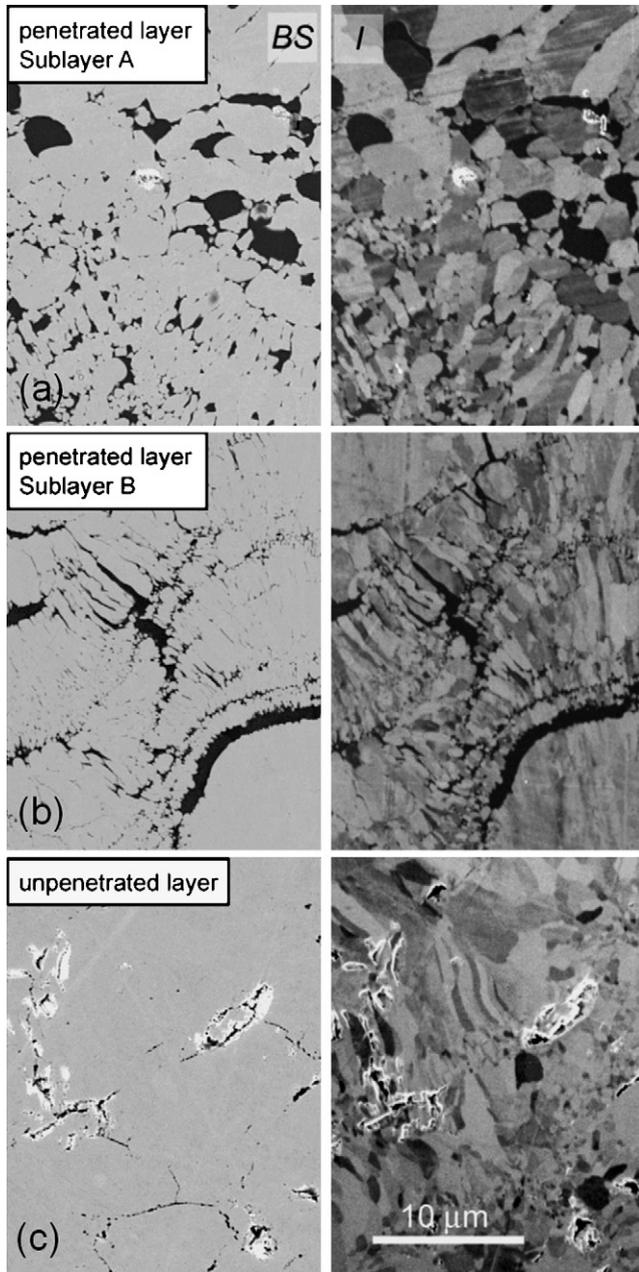
Fig. 6. BS electron (left) and ion images (right) of the microstructures of the two sub-regions within the penetrated zone (a and b) and the corresponding images of the unpenetrated layer (c). The lower sublayer (B) has microstructure comparable to the unpenetrated material except that all of the original void space has been filled with CMAS. Some of the intersplat columnar grain boundaries have been penetrated by the CMAS. In the upper sub-region (A) closest to the surface, the CMAS has spheroidized the TBC grains.

owing to differences in temperature, amount of surface deposits and CMAS composition.

The variation in CMAS composition with depth in zone III (Table 2) suggests a series of melting and infiltration steps consistent with the stochastic nature of the ingestion and deposition of siliceous debris. The composition of the CMAS deep into zone III (depth ~130 μm) is reasonably close to that found on the top of zone I, suggesting that both have similar melting points. Analysis by TEM has revealed a change in the CMAS structure at
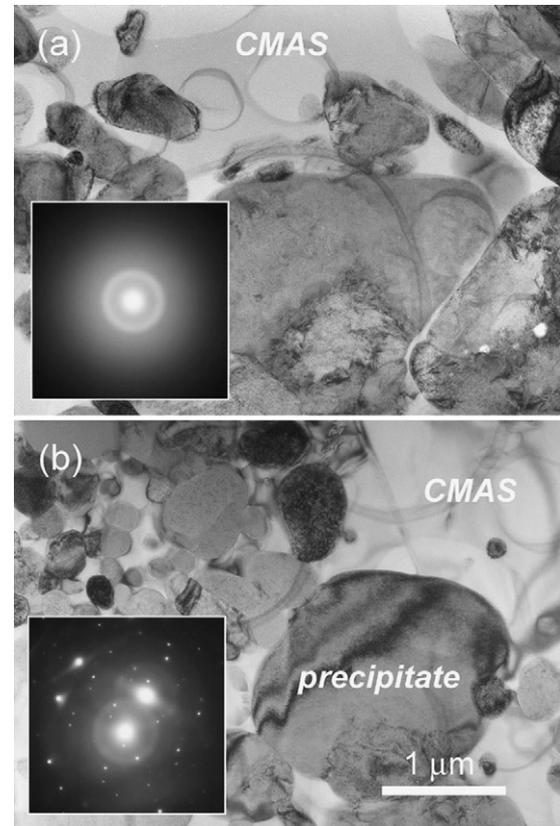

Fig. 7. TEM BF images showing morphology and selected area diffraction pattern from CMAS in: (a) sub-region A (Fig. 6) revealing that the CMAS is amorphous and (b) sub-region B where the CMAS is crystalline.

~150 μm depth (Fig. 7). Close to the surface the CMAS is amorphous (Fig. 7a). Deeper into the coating it is crystalline (Fig. 7b). Large globular particles present at depth ~180 μm (Fig. 7b) are re-precipitated zirconia having the composition given in Table 2: indicating that the CMAS crystallized *after* some dissolution. The TEM samples adjacent to the infiltration front also reveal crystalline CMAS.

The most plausible scenario for the infiltration progressing to a depth $h \approx 500 \, \mu m$ involves the following sequence. *Step I*: at locations where the surface temperature of the TBC exceeds the CMAS melting temperature ($T_M^{CMAS} \approx 1220 \, ^\circ C$), the molten fraction of the deposit penetrates the crevices of the coating. *Step II*: because the temperature of the melt decreases with depth into the coating, the viscous drag increases and the penetration rate diminishes. Nevertheless, for glasses of this chemistry, the viscosity is sufficiently low [13] that penetration can continue well below the isotherm corresponding to T_M^{CMAS}. Indeed, the glass transition temperature of similar glasses ($T_g \approx 800 \, ^\circ C$) [13] implies that a significant layer of under-cooled CMAS is likely to develop within the TBC before the flow becomes sufficiently viscous to fully stop penetration. *Step III*: crystallization within this under-cooled layer commences (perhaps modified by the dissolution of YSZ), constricting the infiltration path and eventually blocking infiltration. In principle, crystallization kinetics would be most active at temperatures in the range, $T_g << T < T_M^{CMAS}$. The implication is that the penetration depth of the CMAS may

correspond to a temperature of order $T_{\text{penetrate}} \approx 1100\,°C$. This expectation is revisited after the temperature gradients in the TBC have been estimated in the following sections.

4. Residual stress estimation

The distribution of residual stress through the thickness of the coating has been estimated by Raman piezo-spectroscopy implemented in an optical microprobe configuration enabling spectra to be obtained with a lateral spatial resolution of 2–3 μm [14]. An Ar/Kr laser operating at 488 nm was used for exciting the Raman spectra whilst minimizing the luminescence from impurity Er^{3+} ions incorporated in the crystal structure of the YSZ. Spectra were recorded using a (Yobin-Yvon) triple mono-chromator. The stress-free frequencies of the Raman peaks for 7YSZ were estimated by recording spectra from powdered fragments of the coating. For polycrystalline zirconia, the piezo-spectroscopy relationship can be expressed as [15]:

$$\Delta \nu_n = \frac{\Pi_n \langle \sigma_1 + \sigma_2 + \sigma_3 \rangle}{3} \tag{1}$$

where the subscript n refers to the Raman peak and the term within $\langle\,\rangle$ refers to the ensemble average of the mean hydrostatic stress. The peak at $\sim460\,cm^{-1}$ is well defined, symmetrical and most readily deconvoluted (see Fig. 8). The piezo-spectroscopic shift of this peak for 5YSZ is $\Pi_n = 5.58\,cm^{-1}/GPa$ [15]. The stress-free relative frequency of the peak for 7YSZ was $\nu_0 \sim 463.68\,cm^{-1}$, almost the same as reported by Bouvier and Lucazeau [15].

The peak shifts in the three zones were obtained by performing a series of measurements on polished cross-sections (e.g. Fig. 5). Care was taken to assure that the stresses were measured at locations midway between adjacent channel cracks in order to provide the closest possible assessment of the misfit stresses that would have existed prior to cracking. The first measurements in each series were taken slightly below the surface ($\sim50\,μm$) to minimize the inevitable scatter associated with the edge of the coating. Each consecutive measurement was taken at 100 μm intervals, with the last measurement close to the bond coat. Six sets of data were recorded in zone III and three each in zones I and II. At each position, several spectra were recorded in order to establish the standard deviation.

The situation in zone III is especially relevant (Fig. 9a). In the penetrated layer near the TBC surface, the peak shift is large with sign indicative of a tensile residual stress. Moreover, this stress increases *linearly in magnitude* with closeness to the surface. In the underlying TBC, the stress is compressive. These characteristics are in accordance with those anticipated by the cracking and delamination patterns (Figs. 2 and 3) and elaborated below. In zones I and II (Fig. 9b), the peak shifts are small, with sign indicative of compression. Over most of the thickness, the shift is spatially invariant.

Converting the peak shift measured on a cross-section into a measure on the in-plane stress level involves several assertions, discussed next, which introduce uncertainties. The stress within the TBC layer before sectioning is biaxial, σ_B. On the cross-section, the stress component normal to the new surface is
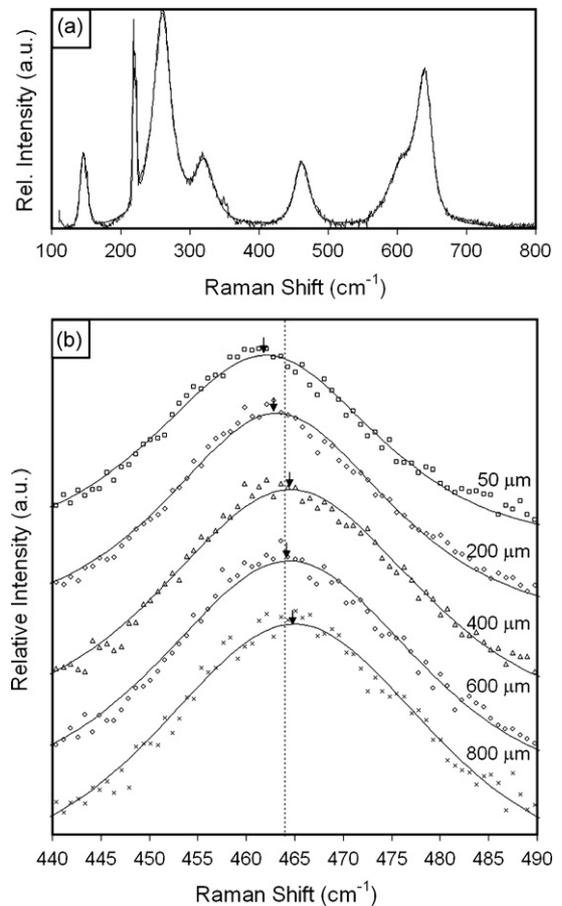

Fig. 8. (a) Raman spectrum indicating that the coating is tetragonal zirconia with no evidence of either the monoclinic or cubic phases. (The sharp peak at $\sim220\,cm^{-1}$ is a plasma line from the laser reflected from the sample.) (b) The fitted E_g Raman peak at $463\,cm^{-1}$ recorded as a function of distance from the top surface. Arrows mark the positions of the maxima.

zero. By eliminating this component, the Poisson effect modifies the stress at the surface parallel to the cross-section to $\sigma_B(1-\nu)$. Thus, provided that the penetration depth of the laser is small (relative to the TBC thickness) the stress probed within the sectioned TBC is, $\langle \sigma_1 + \sigma_2 + \sigma_3 \rangle_{\text{piezo}} = \sigma_B(1-\nu)/3$: $\sigma_3 = \sigma_2 = 0$: whereupon the biaxial misfit stress is related to the frequency shift by, $\sigma_B = [3/(1-\nu)]\Delta\nu_n/\Pi_n$. This stress is that for the YSZ within the splats: not the macroscopic stress in the porous system. Asserting that the stress be qualified by the volume fraction of solid, $1-f$, the stress gradient in the penetrated layer becomes, $|d\sigma_B/dx|_{\text{CMAS}} \approx 1.9\,MPa/μm$. The uncertainties in the zero strain frequency are such that no attempt is made to ascertain the absolute stress levels.

5. Mechanics governing cracking and delamination

To establish a self-consistent thermo-mechanical interpretation of the cracking and delamination phenomena evident in the CMAS penetrated zone, three aspects of the mechanics must be rationalized. (i) The temperatures and thermally induced stresses. (ii) Channel cracking at the surface and the penetration of these cracks into the CMAS-penetrated TBC. (iii) Delamination in the TBC at various levels beneath the surface. Each aspect
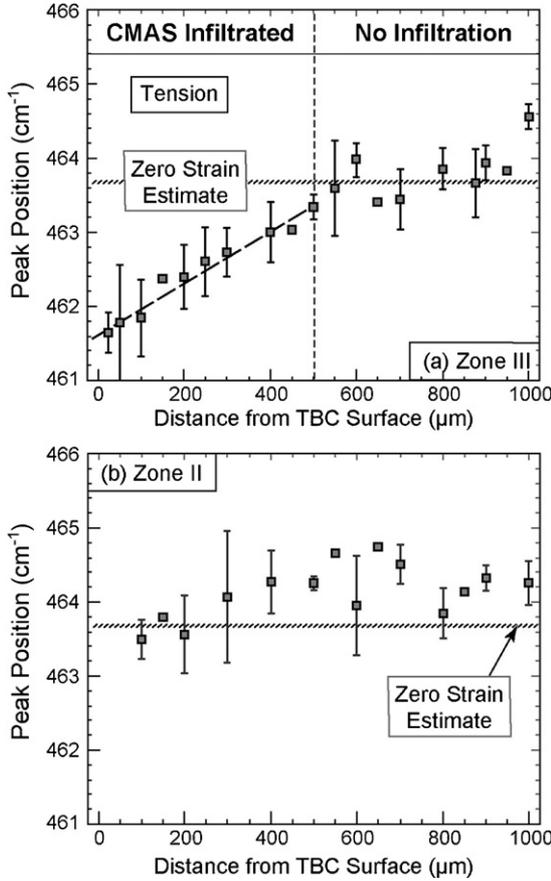
Fig. 9. The Raman peak shifts measured on cross-sections through the shroud. (a) Zone III where the CMAS has penetrated to about 0.5 mm. The stress in the penetrated zone is tensile with steep gradient. Beneath this layer the stress is essentially zero. (b) Zone II with minimal CMAS penetration, revealing small compressive stresses. (Zone I has peak shifts essentially the same as zone II.)

is addressed below. All of the ensuing results are benchmarked against the temperature of the substrate during shroud operation, T_{sub}^0. This temperature is in the range, $800 \le T_{sub}^0 \le 900\,°C$ [16]. The internal consistency of these results and the comparison with the experimental observations is addressed in the following section.

5.1. Thermally induced stresses

During operation, when the shroud is subject to highest heat flux, the surface is at temperature, T_{surf}^0, while the substrate is at T_{sub}^0. The difference is designated, $\Delta T_0 = T_{surf}^0 - T_{sub}^0$ (Fig. 10). The cooling scenario envisages the TBC being on a thick, actively cooled substrate. In the analysis, the TBC has been at the high temperature for a sufficiently long period that any stresses fully relax by creep. Moreover, cooling is sufficiently rapid that the response is everywhere thermo-elastic. The thickness of the CMAS-penetrated zone is designated, h, while the overall TBC thickness is H. The Young's modulus and Poisson ratio of the CMAS penetrated region are, respectively, E_1 and ν_1. The corresponding quantities for the unpenetrated TBC are E_2 and ν_2. The thermal conductivities of the two regions are, k_1 and k_2, respectively. The difference in thermal expansion coeffi-
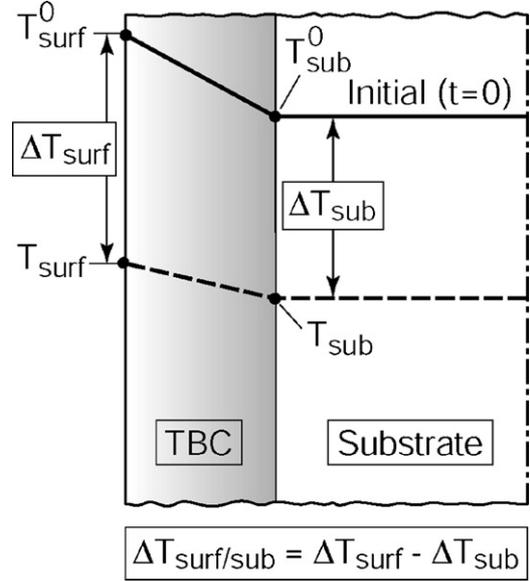
Fig. 10. A thermal scenario considered in the assessment. The salient temperature differences are defined in figure.

cient between the superalloy substrate, α_{sub} and the coating, α, is denoted by $\Delta\alpha = \alpha_{sub} - \alpha$.

The temperature distribution at any instant depends on the thermal conductivities, as well as temperatures at the surface T_{surf} and at the interface with the substrate T_{sub}: where $\eta = x/H$ (with $x = 0$ at the surface and $x = -H$ at the interface with the substrate). In the CMAS penetrated layer ($-h/H \le \eta \le 0$) [12]:

$$T(\eta, t) = T_{surf}(t) + A\eta[T_{surf}(t) - T_{sub}(t)] \tag{2a}$$

and in the TBC below the CMAS ($-1 \le \eta \le -h/H$):

$$T(\eta, t) = T_{sub}(t) + B(1 + \eta)[T_{surf}(t) - T_{sub}(t)] \tag{2b}$$

Here, the non-dimensional coefficients are:

$$
\begin{aligned}
A &= \frac{(k_2/k_1)}{1 - h/H(1 - k_2/k_1)}, \quad -\frac{h}{H} \le \eta \le 0 \\
B &= \frac{1}{1 - h/H(1 - k_2/k_1)}, \quad -1 \le \eta \le -\frac{h}{H}
\end{aligned}
\tag{3}
$$

for $k_2/k_1 = 1$, the variations are strictly linear.

Next we derive an expression for the temperature drop in the penetrated TBC upon cooling. At any stage of cool-down, denote the temperature drop at the surface by, $\Delta T_{surf} = T_{surf}^0 - T_{surf}(t)$, and that at the substrate by, $\Delta T_{sub} = T_{sub}^0 - T_{sub}(t)$. The distribution of the temperature drop can be ascertained directly from (2) [12]. In the CMAS penetrated layer:

$$\Delta T(\eta, t) = (1 + A\eta)\Delta T_{surf/sub}(t) + \Delta T_{sub}(t) \tag{4a}$$

and in the TBC below the CMAS:

$$\Delta T(\eta, t) = B(1 + \eta)\Delta T_{surf/sub}(t) + \Delta T_{sub}(t) \tag{4b}$$

here, $\Delta T_{surf/sub} = \Delta T_{surf} - \Delta T_{sub}$ is the difference between the temperature drop at the surface and that at the substrate, which can vary with time after the start of the cool-down. The in-plane stress, $\sigma(\eta)$, is the sum of one contribution proportional to

$\alpha\Delta T_{\text{surf/sub}}$ and a second proportional to $\Delta\alpha\Delta T_{\text{sub}}$. Namely, in the CMAS penetrated layer [12]:

$$\sigma_B(\eta, t) = \frac{E_1\alpha\Delta T_{\text{surf/sub}}(t)}{1 - \nu_1}\{1 + A\eta - \Phi(t)\} \tag{5}$$

where the dimensionless temperature ratio is

$$\Phi = \frac{\Delta\alpha\Delta T_{\text{sub}}}{\alpha\Delta T_{\text{surf/sub}}}$$

Note that the stress at the surface ($\eta = 0$) is

$$\sigma_{B,\text{surf}}(t) = \frac{E_1\alpha\Delta T_{\text{surf/sub}}(t)}{1 - \nu_1}\{1 - \Phi(t)\} \tag{6}$$

The stress gradient is proportional to $\alpha\Delta T_{\text{surf/sub}}$. In the CMAS penetrated region:

$$H(\mathrm{d}\sigma_B/\mathrm{d}x)|_{\text{CMAS}} = \frac{AE_1\alpha\Delta T_{\text{surf/sub}}}{1 - \nu_1} \tag{7}$$

Thus, the residual stresses at any instant depend on the difference between the cooling of the surface and the cooling of the substrate. Moreover, since the properties of the CMAS-infiltrated layer have yet to be effectively characterized, it is possible to rearrange the foregoing results to eliminate as many of these properties as possible:

$$\Delta T_{\text{surf/sub}} = \frac{\Delta T_{\text{sub}}(\Delta\alpha/\alpha)}{1 - A\sigma_{B,\text{surf}}/H(\mathrm{d}\sigma_B/\mathrm{d}x)} \tag{8}$$

This result will be used below.

5.2. Delamination

Delamination curves can be constructed, as depicted in Fig. 11. The results are for a system with CMAS penetration, $h/H = 0.5$ [12]. They all refer to a 1 mm thick APS–TBC with mode I toughness in the range, $30 \leq \Gamma_{\text{tbc}} \leq 45\,\text{Jm}^{-2}$ and mixed mode toughness [17]:

$$\Gamma(\psi) = \Gamma_{\text{tbc}}[1 + \tan^2((1 - \lambda)\psi)] \tag{9}$$

where Ψ is the phase angle and λ is governed by the ratio of the mode II to mode I toughness (taken to be, $\lambda = 0.25$ [12]). The ordinate in each plot is the *difference* in the temperature drop at the surface and the substrate, which can vary with time after the onset of cooling. The abscissa is the temperature drop experienced by the substrate.

When representative thermal trajectories are superposed, the maximum temperature that can be experienced at the surface of the TBC without forming delaminations is inferred. Depicted in Fig. 12 is a trajectory wherein, during shroud operations, the substrate is at $T_{\text{sub}}^0 \approx 900\,^\circ\text{C}$ and upon shut-down, both the TBC surface and the substrate cool simultaneously. The choice of this trajectory is discussed in the next section. The temperature at which this trajectory intersects each curve gives the maximum allowable temperature difference across the TBC during operation, $\Delta T_{\text{Tbc}}^{\text{Allow}} \equiv \Delta T_{\text{surf/sub}}$, *that averts delamination upon cooling.*
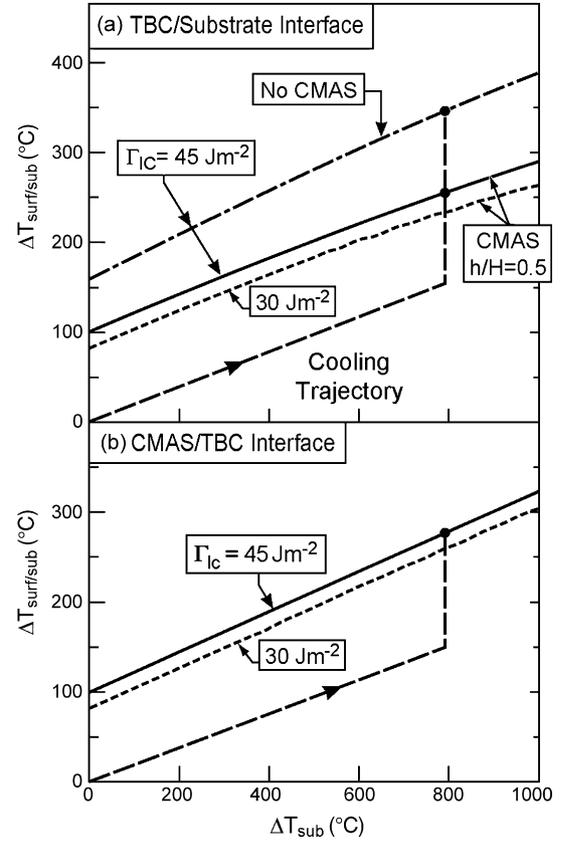

Fig. 11. Delamination curves for a 1 mm thick APS–TBC having representative properties. A representative cooling trajectory is superimposed. The intersection of this trajectory with one of the curves identifies the allowable temperature difference across the TBC, above which the system is susceptible to delamination. (a) Level (i) delamination just above the bond coat. One result is for a TBC without CMAS penetration. The others are for CMAS-penetration depth, $h = 0.5$ mm. (b) Level (ii) delamination along the base of the CMAS-penetrated layer.

5.3. Channel cracking

The tensile stress at the surface of the CMAS-penetrated zone can induce a pattern of channel cracks that extend down through the layer. The spacing between these cracks, s, is governed by the
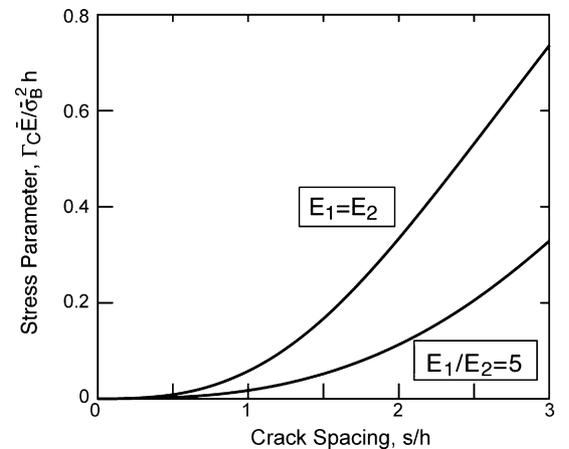

Fig. 12. The relationship governing the spacing between channel cracks and the stress level in the penetrated layer.

level of the stress. An estimate of their spacing can be derived by taking the stress to be uniform and equal to its average, $\bar{\sigma}_B$. The solution is obtained by envisaging a sequential process, wherein the last set of cracks bisects the previous set. The energy release rate for the last set to channel across the layer is given by [18]:

$$G = \frac{\ell \bar{\sigma}_B^2}{\bar{E}_1} \left[2 \tanh \left(\frac{s}{2\ell} \right) - \tanh \left(\frac{s}{\ell} \right) \right] \qquad (10)$$

with

$$\ell = \frac{\pi}{2} g(D)h$$

where D is the Dundurs' parameter [18] and $g(D)$ is the function plotted elsewhere (e.g. Fig. 1 of Ref. [18]). The stress term in (10) should be thought of as the largest tension induced in the CMAS-penetrated TBC at some stage during cool-down.

We bound the spacing by using two choices for the moduli, $E_2 = E_1/5$ and $E_2 \cong E_1$. The corresponding ℓ are [18]:

$$\ell = \left(\frac{\pi}{2} \right) gh = 4h \quad \left(g = \frac{8}{\pi}, \frac{E_2}{E_1} = \frac{1}{5}, D = \frac{2}{3} \right),$$

$$\ell = \left(\frac{\pi}{2} \right) gh = 1.98h \quad \left(g = \frac{3.96}{\pi}, \frac{E_2}{E_1} = 1, D = 0 \right)$$

Since the channel cracks extend through the CMAS within the prior DVCs (Fig. 3c), equating the energy release rate to the mode I toughness of the CMAS, $G = \Gamma_{CMAS}$ gives the implicit solution:

$$\frac{\bar{E}_1 \Gamma_{CMAS}}{\bar{\sigma}_B^2 h} = \frac{\pi}{2} g(D) \left[2 \tanh \left(\frac{s}{\pi gh} \right) - \tanh \left(\frac{s}{(\pi/2)gh} \right) \right] \qquad (11)$$

The results are plotted in Fig. 12.

6. Assessment and implications

In this section the preceding results are assembled and critically assessed. The challenges are that the properties of the CMAS-infiltrated layer can only be estimated and the exact cooling trajectory is unknown. We commence with the guidance that both the TBC surface and the substrate cool simultaneously, as indicated in Fig. 11. For this case, inserting the temperature drops into Eq. (6) indicates that *the maximum tension at the TBC surface exist at ambient*. Namely, the tension is lower at all other stages of the cool-down. Moreover this maximum is given by

$$\sigma_{B,surf}^{max} = \frac{E_1}{1 - \nu_1} \left[\alpha \Delta T_{surf/sub} - \Delta \alpha \Delta T_{sub} \right] \qquad (12)$$

The significance of this assertion is that the stress estimate from the crack spacing, $\bar{\sigma}_B$ (Fig. 12) and the stress gradient estimate from the Raman, $d\sigma_B/dx$ (Section 4) can be combined to assess the temperature gradients upon assuming that the channel cracks extend through the penetrated layer. The connection is given by

$$\sigma_{B,surf}^{max} = \bar{\sigma}_B + (1/2)h \frac{d\sigma_B}{dx} \qquad (13)$$

Starting with the channel crack spacing, $s/h \approx 2$, and superimposing in Fig. 12 indicates that: $\bar{\sigma}_B^2 h / \bar{E} \Gamma_{CMAS} = 10$. To utilize the channel cracking solution, some *assertions* are needed regarding the properties of the CMAS-penetrated layer. (i) One is that the CMAS has toughness somewhere between values typical of those for glasses and polycrystalline oxides, $10 \, \text{Jm}^{-2} \lesssim \Gamma_{CMAS} \lesssim 20 \, \text{Jm}^{-2}$ [19,20]. (ii) Another is that the elastic modulus is close to that for dense YSZ, $E_1 = 200 \, \text{GPa}$, because it is the predominant micro-structural constituent. With these choices, the average stress is ascertained to be in the range $200 \, \text{MPa} \lesssim \bar{\sigma}_B \lesssim 280 \, \text{MPa}$. Inserting these stresses into (13) and using $|d\sigma_B/dx|_{CMAS} \approx 1.9 \, \text{MPa/}\mu\text{m}$ (based on the Raman measurements: Fig. 9), the tension at the surface at ambient would be in the range $675 \, \text{MPa} \lesssim \sigma_{B,surf}^{max} \lesssim 775 \, \text{MPa}$, depending upon the choice for the CMAS toughness.

These stresses may now be used with (8) to estimate the unknown temperature difference across the TBC during operation, $\Delta T_{surf/sub}$, within zone III, subject to independent information about the operating temperature of the substrate, T_{sub}^0. By using the thermal expansions, $\alpha = 11 \, \text{ppm/}^{\circ}\text{C}$, $\Delta \alpha = 4 \, \text{ppm/}^{\circ}\text{C}$ and assuming, $k_1 \approx 2k_2$, such that $A = 2/3$ (namely, the penetrated layer has twice the conductivity of the unaffected TBC), this difference becomes, $\Delta T_{surf/sub}/T_{sub} = 0.42$ and 0.53 for the two extremes of the toughness range. If $T_{sub}^0 = 900 \, ^{\circ}\text{C}$ [16], the temperature difference across the TBC would be in the range $380–480 \, ^{\circ}\text{C}$. The corresponding temperatures of the TBC surface during operation would be in the range $T_{surf} = 1280$ and $1380 \, ^{\circ}\text{C}$, respectively. Both exceed the CMAS melting temperature ($T_M^{CMAS} = 1220 \, ^{\circ}\text{C}$) and thus consistent with the extent of the CMAS-penetration in zone III, discussed in Section 3.

Finally, for the delamination mechanics to be consistent with the observations (Fig. 2), the following must emerge. In zone III, where the CMAS has penetrated and delaminations are in evidence, the allowable, ΔT_{tbc}^{Allow} must be less than the difference between the surface temperature and substrate temperatures: that is, the inequality:

$$\Delta T_{tbc}^{Allow} < T_{surf}^0 - T_{sub}^0 \qquad (14a)$$

must be satisfied. With $h/H = 0.5$, Fig. 11a gives an allowable, $\Delta T_{tbc} = 250 \, ^{\circ}\text{C}$ for level (i) delamination: while Fig. 11b gives $\Delta T_{tbc} = 220 \, ^{\circ}\text{C}$ for level (ii). Given the foregoing assessment that $\Delta T_{surf/sub} \geq 380 \, ^{\circ}\text{C}$, both satisfy condition (10). In zones I and II, where there is no CMAS penetration and delaminations are not in evidence, the allowable should satisfy:

$$\Delta T_{tbc}^{Allow} \geq T_M^{CMAS} - T_{sub}^0 \qquad (14b)$$

The results from Fig. 11a infer that $\Delta T_{tbc}^{Allow} = 360 \, ^{\circ}\text{C}$ compared with $T_M^{CMAS} - T_{sub}^0 = 320 \, ^{\circ}\text{C}$, satisfying (14b). Accordingly, the delamination maps (Fig. 11) provide predictions consistent with the measurements. The caveat is that several assertions have been made and several properties estimated. Future assessments will address the fidelity of these implications through property measurements on CMAS-infiltrated YSZ and by additional measurements of stress gradients.

7. Concluding remarks

The susceptibility of TBC hot-section components to cracking and delamination when penetrated by CMAS has been examined. The assessment has been based on stationary components removed from aero-engines with relatively thick (1 mm) TBCs deposited by atmospheric plasma spray. In zones that experience the highest temperatures the CMAS melts, penetrates to a depth of about 0.5 mm and infiltrates all open areas. In such zones, the TBC contains channel cracks and sub-surface delaminations, as well as spalls.

The ambient temperature residual stress gradients in the CMAS-penetrated zones have been measured on cross-sections by using the Raman peak shift. These indicate tensile stresses at the surface, becoming compressive below, with gradient, 1.9 MPa/μm. Measurements of the spacing between (surface-connected) channel cracks have provided an independent measure of the average stress within the penetrated layer. Together these measurements indicate that the tensile stress at the surface is about 700 MPa: upon assuming a thermal scenario wherein the surface and substrate cool simultaneously (no thermal shock).

In turn (and upon using the same thermal scenario) these stresses have been used to assess the temperature gradient experienced by the TBC during operation in the turbine. In the CMAS-penetrated zone, these temperature differences are determined to be the range 380–480 °C, consistent with a temperature at the surface that exceeds that for CMAS melting by up to 160 °C. By invoking the relevant mechanics, the likely incidence of delamination at the two primary locations (just above the bond coat and at the base of the CMAS-penetrated layer) has been evaluated and shown to be consistent with the thermal gradient that exists during turbine operation, as well as the proposed cooling scenario. Continued assessments in this area would benefit from systematic measurements of the thermo-mechanical properties of the CMAS-penetrated TBC, as well as experiments conducted with well-delineated temperature histories. Definitive conclusions regarding the precise role of CMAS penetration on the incidence of delamination await these additional measurements and tests.

Acknowledgements

References

[1] M.P. Borom, C.A. Johnson, L.A. Peluso, Surf. Coat. Technol. 86–87 (1996) 116–126.
[2] C. Mercer, S. Faulhaber, A.G. Evans, R. Darolia, Acta Mater. 53 (2005) 1029–1039.
[3] S. Krämer, J. Yang, C.A. Johnson, C.G. Levi, J. Am. Ceram. Soc. 89 (10) (2006) 3167–3175.
[4] A.G. Evans, D.R. Mumm, J.W. Hutchinson, G.H. Meier, F.S. Pettit, Prog. Mater. Sci. 46 (2001) 505–553.
[5] D.R. Clarke, C.G. Levi, Annu. Rev. Mater. Res. 33 (2003) 383.
[6] T.E. Strangman, Thin Solid Films 127 (1985) 93–105.
[7] T. Xu, S. Faulhaber, C. Mercer, M. Maloney, A.G. Evans, Acta Mater. 52 (2004) 1439–1450.
[8] R. Vassen, F. Traeger, D. Stover, J. Therm. Spray Technol. 13 (3) (2004) 396–400.
[9] T.A. Taylor, Thermal barrier coating for substrates and process for producing it, U.S. Patent 5,073,433 (1991).
[10] D.M. Gray, Y.C. Lau, C.A. Johnson, M.P. Borom, W.A. Nelson, Thermal barrier coatings having an improved columnar microstructure, U.S. Patent 6,180,184 B1 (2001).
[11] A.A. Kulkarni, A. Goland, H. Herman, A.J. Allen, J. Ilavsky, G.G. Long, C.A. Johnson, J.A. Ruud, J. Am. Ceram. Soc. 87 (7) (2004) 1294–1300.
[12] A.G. Evans, J.W. Hutchinson, Surf. Coat. Technol. 201 (2007) 7905–7916.
[13] D. Giordano, D.B. Dingwell, J. Phys.: Condens. Mat. 15 (2003) S945–S954.
[14] A.M. Limarga, D.R. Clarke, Piezo-spectroscopic coefficients of tetragonal prime yttria-stabilized zirconia, J. Am. Ceram. Soc. 90 (4) (2007) 1272–1275.
[15] P. Bouvier, G. Lucazeau, J. Phys. Chem. Solids 61 (2000) 569–578.
[16] GE Aircraft Engines, private communication.
[17] J.W. Hutchinson, Z. Suo, Z. Adv. Appl. Mech. 29 (1992) 63–191.
[18] C. Xia, J.W. Hutchinson, J. Mech. Phys. Solids 48 (2000) 1107–1131.
[19] J.B. Wachtman, Mechanical Properties of Ceramics, Wiley, New York, 1996.
[20] B.R. Lawn, Fracture of Brittle Solids, Cambridge University Press, Cambridge, 1993.